International Journal of Heat and Mass Transfer 124 (2018) 319–330

Contents lists available at ScienceDirect

International Journal of Heat and Mass Transfer

journal homepage: www.elsevier.com/locate/ijhmt

A comparison study on the thermal effects in DBD plasma actuation and electrical heating for aircraft icing mitigation

Yang Liu, Cem Kolbakir, Haiyang Hu, Hui Hu *

Department of Aerospace Engineering, Iowa State University, 2271 Howe Hall, Room 1200, Ames, IA 50011, USA

ARTICLE INFO

Article history:
Received 30 November 2017
Received in revised form 5 February 2018
Accepted 22 March 2018

Keywords:
DBD plasma
Electrical heating
Icing physics
Aircraft icing mitigation

ABSTRACT

A comparison study of a novel method of utilizing thermal effects induced by Dielectric-Barrier-Discharge (DBD) plasma actuation (*i.e.*, DBD plasma-based method) and a conventional electrical heating method for aircraft icing mitigation was performed in an Icing Research Tunnel available at Iowa State University (*i.e.*, ISU-IRT). A NACA0012 airfoil/wing model embedded with an AC-DBD plasma actuator and a conventional electrical film heater over the airfoil surface was tested under a typical aircraft icing condition. While a high-speed imaging system was used to record the dynamic ice accretion and transient surface water transport processes over the airfoil surface, an infrared (IR) thermal imaging system was also utilized to map the corresponding surface temperature distributions over the airfoil surface simultaneously to quantify the unsteady heat transfer and phase changing process over the ice accreting airfoil surface. It was found that, with the same power input, the DBD plasma-based method showed at least equivalent effectiveness, if not better, in preventing ice accretion over the airfoil surface, in comparison to the conventional electrical heating method. Further optimization of the DBD plasma-based method with a duty-cycle modulation was found to have a much better anti-/de-icing performance, in comparison to the conventional electrical heating method. The findings derived from the present study demonstrated the potential of a new class of anti-/de-icing strategy by leveraging the thermal effects induced by DBD plasma actuation for aircraft in-flight icing mitigation.

1. Introduction

Ice accretion on aircraft surfaces has been widely recognized as a significant safety hazard in cold weathers, especially when aircraft travel through clouds with supercooled water droplets suspended. Many aviation accidents have been reported attributing to ice accretion on aircraft. Petty and Floyd [1], who summarized the accidents caused by aircraft icing, and found that there were more than 800 fatalities resulting from ice accumulations in the past 20 years. Depending on the flight conditions and environmental parameters, the in-flight ice accretion can be either *rime* or *glaze* [2]. When the ambient temperature is relatively cold (*i.e.*, typically below −10 °C) and the airflow is dry with a lower liquid water content (*LWC*), supercooled water droplets would freeze immediately upon impact on the aircraft surface, forming *rime* ice. At warmer temperatures, *i.e.*, just below the water freezing temperature, if the *LWC* level in the airflow is relatively high, the impinged supercooled water droplets would freeze partially, with the remaining water mass transporting along the surface prior to freezing downstream, forming much complex ice shapes, which is called *glaze* ice. Because of its wet nature, *glaze* ice tends to extend further and substantially deform the ice accreting surface with the formation of "horns" growing outward in the airflow, causing large scale flow separations. *Glaze* icing is considered to be more dangerous since it usually leads to much more dramatic increases in drag and decreases in lift [3]. Although many efforts have been made in recent years [4–11], aircraft icing remains an important unsolved problem that is threatening the aviation safety.

While a number of anti-/de-icing systems have already been developed and implemented for aircraft icing mitigation, *i.e.*, freezing-point depressants, thermal melting, and surface deformation [12], current anti-/de-icing strategies suffer from various drawbacks. For example, aqueous solutions of propylene and ethylene glycol (minimum of 50% concentration) along with other chemical additives are widely used for aircraft anti-/de-icing at airports [13]. Propylene and ethylene glycol, although readily biodegradable, exert an extremely high biochemical oxygen demand on aquatic systems that result in killing fish and other aquatic creatures due to the depletion of dissolved oxygen [14]. There has been an increasing concern of the environmental impacts from the aircraft anti-/de-icing fluid swept away with

* Corresponding author.
E-mail address: huhui@iastate.edu (H. Hu).

https://doi.org/10.1016/j.ijheatmasstransfer.2018.03.076
0017-9310/

storm and melt water runoff at airports to ground water and nearby waterways [15]. Pneumatic de-icing systems with rubber boots have been used to break off ice chunks accreted at airfoil leading edge for aircraft in-flight icing mitigation, but they are usually very heavy and sometimes unreliable [16]. Ultrasonic and mechanical de-icing solutions are not easily integrated into existing aircraft and pose foreign object damage (FOD) hazards to engines [16]. While electro-thermal de-icing systems have also been used to melt out ice by heating aircraft wing surfaces, they are usually very inefficient and have demanding power requirements, and can also cause damage to composite materials from overheating. Furthermore, the melted water may simply run back and re-freeze at a downstream location to cause uncontrolled ice accretion [16]. In looking to improve the operational performance of aircraft in cold weathers, methods and techniques for more efficient anti/de-icing performance but with less complexity and adverse environmental impacts are highly desirable.

Dielectric barrier discharge (DBD) plasma actuation is a type of discharge producing an ionized gas at the dielectric surface by the application of high amplitude and high frequency of Alternative Current (AC) voltage (*i.e.,* AC-DBD) or nanosecond-scale pulsed voltage (*i.e.,* ns-DBD) between two electrodes separated by a dielectric layer. The use of DBD plasma actuators for active flow control has gained significant interest in the aerospace engineering community [17,18], with its unique advantages including absence of moving components, fast response time, easy implementation and stable operation. Fig. 1 shows schematically a general configuration of a DBD plasma actuator, which has two electrodes (*i.e.*, exposed electrode *vs*. encapsulated electrode) attached to the opposing surfaces of a dielectric barrier material. For AC-DBD plasma actuation, powered by an alternating current, ionized air molecules are formed in the discharge region above the encapsulated electrode, inducing a small fluid velocity adding momentum to the boundary layer. For ns-DBD plasma actuation, they usually induce an ultrafast gas heating mechanism eventually leading to the generation of a shock wave [19–22]. The plasma discharge generates an ionic airflow along the surface of the dielectric layer, which has been widely used for flow manipulation such as separation control on airfoils [23–25] and delay/promotion of boundary layer transition [26,27]. Therefore, DBD plasma actuators are usually designed to be located at the regions where the aerodynamic characteristics alter greatly as incoming flow changes, e.g., airfoil leading edges and duct lips of aero-engines. It should be noted that, such aerodynamically delicate regions are always the preferential sites of in-flight ice accretion in cold weathers [28]. Inspiringly, DBD plasma actuators have also been revealed to have significant thermal effects along with the ionic wind generation [29,30], which can be utilized for icing control as an additional function of the DBD plasma actuators.

As revealed by Stanfield et al. [29] and Dong et al. [30], during a DBD plasma discharge, the rotational temperature of the gas above the grounded electrode of the DBD actuator can be up to 200 °C, while the vibrational temperatures were observed to be an order of magnitude higher than the rotational temperature. They also found that the primary mechanism for the heating of the dielectric layer is through heat transfer from the plasma, *i.e.*, through direct injection, convection and radiation, while only a small portion is contributed to the power dissipation within the dielectric layer. Previous studies also revealed that the maximum temperatures are always located near the edge of the exposed high-voltage electrode [31]. To further characterize the thermal effects of DBD plasma discharge, Tirumala et al. [32] conducted infrared thermography measurements on the surface of a thick dielectric DBD plasma actuator. It was found that the predominant mechanism of dielectric heating is due to the heat transfer from the plasma to the gas which then heats up the dielectric surface through forced convection. The increase in temperature was found to have linear relationship with both the applied voltage and the input frequency. Adopting the thermal effects of DBD plasma actuation, Zhou et al. [28] conducted a feasibility study to investigate the anti-/de-icing performance of an AC-DBD plasma actuator on an ice accreting airfoil model, and found that the AC-DBD plasma actuator was very effective in anti-icing operations. Recently, a ns-DBD plasma actuator was also examined in the de-icing operation of an iced plate [33]. With the ultrafast heating process of the ns-DBD plasma actuator, the ice layer formed on the test plate was effectively removed. In spite of the advances made in the development of DBD plasma actuators for icing control [28,33], the thermal physics of DBD plasma discharge and its applicability for aircraft in-flight icing mitigation, especially about the anti-/de-icing performance of a DBD plasma-based method in comparison with those of conventional electrical heating strategies, remain unexplored. With this in mind, we conducted an experimental study to evaluate the anti-/de-icing performance of a DBD plasma-based method, in comparison to that of a conventional electrical heating method, for aircraft in-flight icing mitigation applications.

In the present study, while an AC-DBD plasma actuator was fabricated and implemented over one half side of an NACA 0012 airfoil/wing model, a conventional electrical film heater was flush mounted on the other half side of the airfoil/wing model (i.e., side by side with the DBD plasma actuator). An experimental investigation was conducted to provide a side-by-side comparison between the DBD plasma actuator and the conventional electrical film heater in preventing the ice formation and accretion over the airfoil surface under a typical glaze icing condition. The experimental study was conducted in a unique Icing Research Tunnel available at Iowa State University (*i.e.*, ISU-IRT). While a high-speed camera was used to capture the transient details of the dynamic ice accretion and water transport processes over the airfoil surface, an infrared thermal imaging system was utilized to map the surface temperature evolutions during the dynamic ice accretion process and/or anti-/de-icing process with the AC-DBD plasma and the electrical film heater turned on. The temporally-synchronized-and-resolved measurements enabled the correlation between the icing-morphology and surface temperature distributions, which was used to elucidate the underlying physics pertinent to the thermal energy transfer in the DBD plasma actuation process, thereby, to improve our understanding about the working mechanism of the DBD plasma-based method for aircraft icing mitigation.

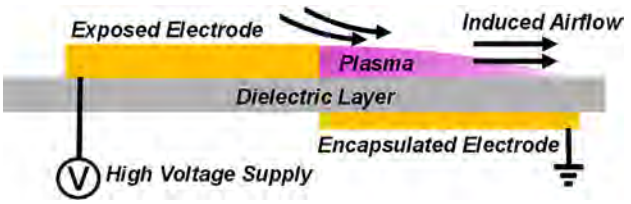

Fig. 1. A DBD plasma actuator with two electrodes attached to the opposing surfaces of a dielectric layer.

2. Experimental setup and test model

The comparison study of AC-DBD plasma actuation and electrical film heating methods for icing mitigation was performed in a unique Icing Research Tunnel available at Aerospace Engineering Department of Iowa State University (*i.e.*, ISU-IRT) [7]. As shown schematically in Fig. 2, ISU-IRT is a multifunctional icing research tunnel with a test section of 2.0 m in length × 0.4 m in width ×

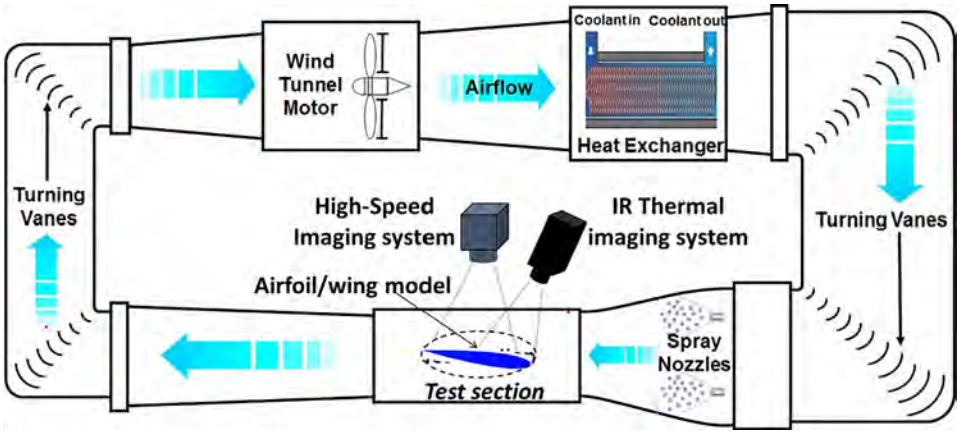

Fig. 2. A schematic of the icing research tunnel and experimental setup used in the present study.

0.4 m in height with four side walls being optically transparent. It has a capacity of generating a maximum wind speed of 60 m/s and an airflow temperature down to −25 °C. An array of 8 pneumatic atomizer/spray nozzles are installed at the entrance of the contraction section of the icing tunnel to inject micro-sized water droplets (10–100 μm in size with a MVD ≈ 20 μm) into the airflow. By manipulating the water flow rate through the spray nozzles, the liquid water content (*LWC*) in ISU-IRT could be adjusted (*i.e.*, *LWC* ranging from 0.1 g/m^3 to 5.0 g/m^3). In summary, ISU-IRT can be used to simulate atmospheric icing phenomena over a range of icing conditions (*i.e.*, from dry *rime* to extremely wet *glaze* ice conditions).

A NACA 0012 airfoil/wing model was used in the present study, which was made of a hard-plastic material and manufactured by using a rapid prototyping machine (*i.e.*, 3-D printing) that builds 3-D models layer-by-layer with a resolution of about 25 μm. The wing model has a chord length of $c = 150$ mm, which spanned the width of the test section of ISU-IRT. Supported by a stainless-steel rod, the airfoil/wing model was mounted at its quarter-chord and oriented horizontally across the middle of the test section.

Fig. 3 shows the schematic of the AC-DBD plasma actuator and the electrical film heater embedded over the NACA0012 airfoil/wing model. The plasma actuator consisted of four encapsulated electrodes and five exposed electrodes, with the same thickness of about 70 μm. In the present study, three layers of Kapton film (*i.e.*, 130 μm for each layer) were integrated to serve as the dielectric barrier to separate the encapsulated electrodes from the exposed electrodes. Ranging from the leading-edge position to about 27% chord length of the airfoil model, four encapsulated electrodes were distributed evenly along the airfoil model with a separation distance of 3 mm. The length of the encapsulated electrodes was about 350 mm, and the width was 10.0 mm (except the one at the leading edge which was 5.0 mm). As reported by Waldman and Hu [7], since most of the ice would be formed around the leading edge of the airfoil/wing model, the width of the first encapsulated electrode was reduced to 5.0 mm in order to generate more plasma near the airfoil leading-edge for a successful anti-/de-icing operation in the region, while the encapsulated electrodes were attached symmetrically around the leading edge of airfoil. As for the exposed electrodes (*i.e.*, 96 mm in length and 3.0 mm in width), they were placed right above the covered electrodes with zero overlap between the exposed and encapsulated electrodes. As clearly shown in Fig. 3, an electrical film heater (*i.e.*, Kapton® Polyimide Film insulated heater, which was selected due to its good operational performance among the electrical film heaters available on the market) was embedded on the other half side of the surface of the airfoil/wing model. The electrical film heater consists of an

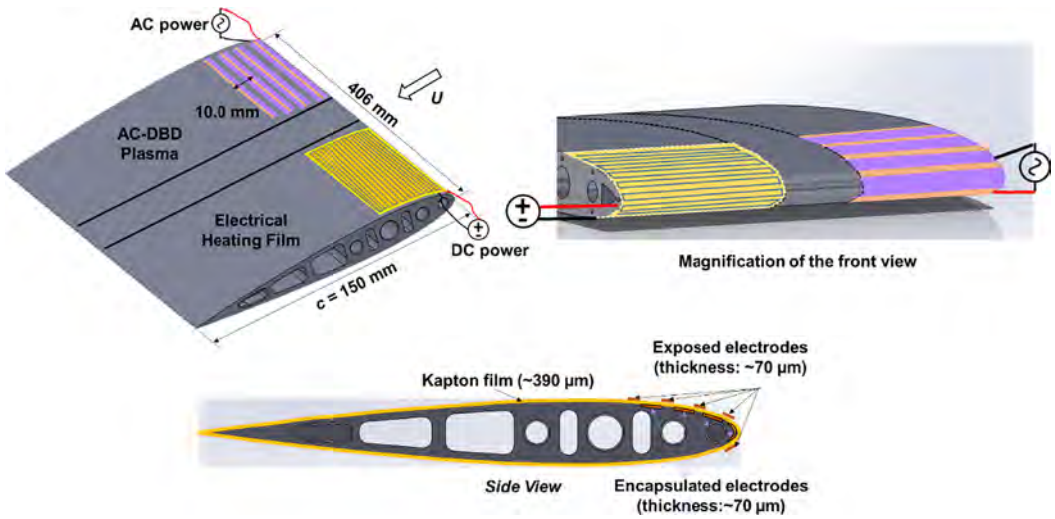

Fig. 3. Schematic of a NACA 0012 airfoil/wing model with the AC-DBD plasma actuator and electrical film heater attached side-by-side on the surface.

etched foil element of 0.013 mm thickness that is encapsulated between two layers of 0.05 mm Polyimide Film and 0.025 mm FEP adhesive tape. The coverage area of the film heater is 50.8 mm × 101.6 mm. As shown in Fig. 3, a DC power source was used to power the electrical film heater.

In the present study, a typical glaze icing condition was generated in ISU-IRT as described in 14 CFR Part 25 Appendix C [36] (*i.e.,* with the freestream air velocity of U_∞ = 40 m/s, LWC = 1.0 g/m^3, and airflow temperature of T_∞ = −5 °C). The angle of attack (α) of the airfoil model was set at α = 0° during the experiments. The DBD plasma actuator was wired to a high-voltage AC power supply (Nanjing Suman Co., CTP-2000 K), which can provide a maximum 30 kV peak-to-peak sinusoidal voltage with a center frequency of 10 kHz. While the AC current applied to the plasma actuator was measured by using a high response current probe (Pearson Electronics, Inc., Pearson 2877), the high-amplitude voltage was measured by using a high voltage probe (P6015A from Tektronix), and monitored by an oscilloscope (Tektronix DPO3054). The voltage of the sinusoidal excitation to the electrodes was manipulated with a variable voltage transformer at a constant frequency of 10 kHz. During the experiments, to quantitatively compare the operational performance of the AC-DBD plasma actuator and the electrical film heater under different icing conditions, the applied power (or power density, P_d) to the plasma actuator was adjusted to be equivalent with that applied to the electrical film heater. Table 1 summarizes the experimental parameters used in the present study.

During the experiments, the dynamic ice accreting process over the airfoil surface was recorded by using a high-speed camera (PCO Tech, Dimax) with a 60 mm lens (Nikon, 60 mm Nikkor f/2.8) installed at 500 mm above the airfoil/wing model. The camera was positioned approximately normal to the airfoil chord, with a measurement window size of 210 mm × 210 mm and a spatial resolution of 9.5 pixels/mm. An in-situ calibration procedure as suggested by Soloff et al. [34] was performed to dewarp the captured images before extracting physical features. Each test trial consisted of 3000 images acquired at a frame rate of 10 Hz.

As shown in Fig. 2, an infrared (IR) thermal imaging camera (FLIR A615) was also used to map the surface temperature of the ice accreting airfoil. The IR camera was mounted at ~300 mm above the airfoil/wing model with a measurement window size of 110 mm × 90 mm and a corresponding spatial resolution of 5.3 pixels/mm. Radiation from the ice accreting airfoil surface will pass through an infrared window (*i.e.*, FLIR IR Window-IRW-4C with optic material of Calcium Fluoride) at first before reaching to the IR camera. A calibration of the material emissivity is performed for the IR thermal imaging [35]. Table 2 gives the IR emissivity coefficients of the materials relevant to the present study, *i.e.*, material of the airfoil/wing model, ice, and liquid water, respectively. Each test trial consisted of 15,000 IR images acquired at a frame rate of 50 Hz. An in-situ calibration was also performed to validate the IR thermal imaging results by establishing a relationship between the measured count number from the IR camera and the temperature acquired by using thermocouples. The measurement uncertainty for the IR camera was found to be less than 0.5 °C. The high-speed video camera and the IR camera were connected to a digital delay generator (Berkeley Nucleonics, model 575) that synchronized the timing between the two systems.

Table 2
Emissivity of the materials pertinent to the test model used in the present study.

Materials	Emissivity
Surface of the airfoil/wing model (Enamel coated)	0.960
Ice	0.965
Water	0.950–0.963

3. Results and discussion

3.1. Electrical characteristics of the AC-DBD plasma actuator before and during ice accretion

Since a multiphase interaction (*i.e.,* water–ice-air-plasma interaction) would occur during the operations of the AC-DBD plasma actuator under icing conditions, the effect of the water impingement on the electrical characteristics of the AC-DBD plasma actuator was first evaluated. Fig. 4 shows the measured voltage and current traces as a function of time within six AC cycles before and during the ice accretion process (*i.e.*, U_∞ = 40 m/s, T_∞ = −5 °C and LWC = 1.0 g/m^3). Before the supercooled water droplets impinged onto the airfoil surface, the exposed electrodes and the dielectric surfaces were free of water/ice, typical voltage and current traces of DBD plasma discharge were observed as clearly shown in Fig. 4(a), with the large spikes dominating the current curve, indicating the micro-discharges in the plasma discharge region over the surface of the dielectric layer.

Since the surfaces of the exposed electrodes and the dielectric layer had been heated sufficiently during the DBD plasma actuation, after impingement of the supercooled water droplets onto the airfoil surface, the impinged super-cooled water droplets were found to be heated up quickly to form liquid water films/rivulets and run back over the heated airfoil surface (*i.e.,* surfaces of exposed electrodes and dielectrics layer). The presence of such water mass over the electrode/dielectric surfaces was suggested to have a great impact on the electrical characteristics of the plasma actuator (*i.e.,* with the runback water becoming the conductor extension of the exposed electrodes in AC-DBD plasma actuation [37]). Fig. 4(b) shows the measured voltage and current traces of the AC-DBD plasma actuator during the ice accretion process. It can be seen clearly that, while the voltage signal was almost not changed, the amplitude of the large spikes in the current trace was found to be significantly reduced, which is suggested to be caused by the less glow discharge at the running water film/rivulets fronts. Based on the measured voltage and current traces as that shown in Fig. 4, the power density, q, of the plasma actuator can be calculated using following equation:

$$q = \frac{1}{nR \cdot A} \int_{nR} V(t) \cdot I(t) dt \tag{1}$$

where R is the AC period of plasma actuation, n is the number of AC cycles, and A is the reference area.

3.2. Thermal effects of AC-DBD plasma actuation

Recent studies [26,29–32] have demonstrated that DBD plasma actuators have significant thermal effects along with the generation of ionic airflow. With the high-voltage signal applied to the exposed electrode, a high-intensity electric field is generated

Table 1
Experimental parameters used in the present study.

U_∞	T_∞	LWC	$V_{p\text{-}p}$	f	P_{input}	P_d
40 m/s	−5 °C	1.0 g/m^3	5–20 kV	10 kHz	40–80 W	7.8–15.6 kW/m^2

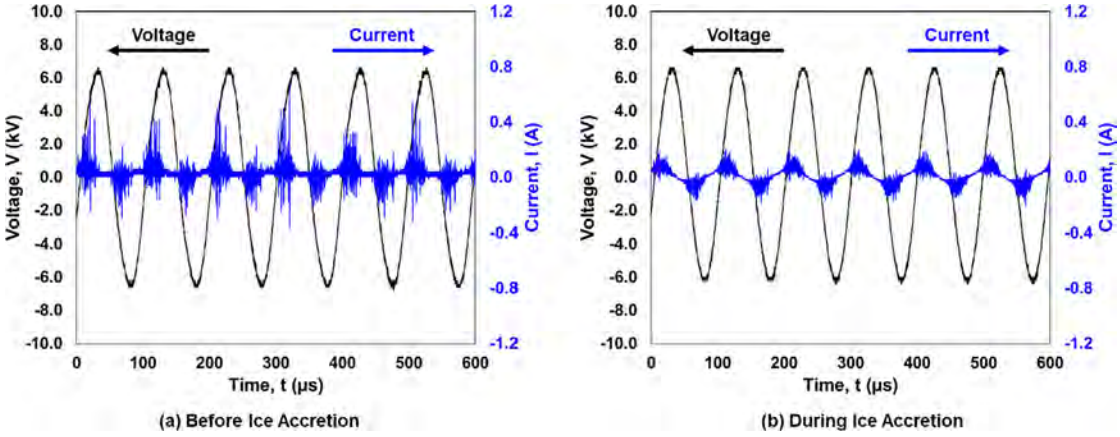

Fig. 4. Measured voltage and current traces of the AC-DBD plasma actuator within six AC cycles before and during the ice accretion process.

between the exposed electrode and the grounded electrode separated by a dielectric layer. Driven by the electric field, the free electrons and ions in the air are responsible for energy transmission from the external power source to gas [32,38]. The free electrons get energy from the electric field through acceleration, and then collide with neutrals and ions in the air. If an elastic collision occurs, there is an immediate but only a small portion of total energy release, while in inelastic collisions, ionized particles and excited molecules can be produced, which are the main sources of energy heating the gas [38]. Collision between ions and neutrals/electrons is another source that contributes to the thermal energy generation in DBD plasma actuation [39]. Therefore, the thermal energy generated during plasma discharge can be expressed using Eq. (2):

$$E_{heat} = E_{ele} + E_{ion} \tag{2}$$

where E_{heat} denotes the thermal energy generated in plasma discharge, E_{ele} is the energy released through collision between electrons (*i.e.*, accelerated in electric field) and neutrals or ions, and E_{ion} is the energy released through collision/quenching between ions and neutrals or free electrons.

In a recent study conducted by Rodrigues et al. [40], it was also found that, for lower voltage supplies at which there is no plasma formation, the input energy is almost equal to the thermal energy dissipated into the dielectric layer. It was suggested that at such low voltage levels, the energy applied to the plasma actuator can be completely converted into dielectric heating since there is no plasma formation and momentum transfer to the surrounding air.

Fig. 5 shows the time evolution of the measured temperature distribution over the surface of the airfoil/wing model after the AC-DBD plasma actuator was switched on at $V_{p\text{-}p}$ = 12.5 kV and f = 10 kHz under the test condition of U_∞ = 40 m/s, T_∞ = −5 °C, and LWC = 0 g/m^3 (*i.e.*, without turning on the spray system of the ISU-IRT). It is clearly seen that, after the plasma actuator was switched on, the surface temperatures over the dielectric layer and the exposed electrodes were increased rapidly, with the local surface temperatures at the edges of the exposed electrodes being increased from −5 °C to more than 25 °C in less than five seconds. The temperature distribution pattern was found to be rather uniform along the span-wise, as expected. It has been reported in the previous studies [41] that the response time of momentum transfer in plasma discharge is on the order of 10–100 ms. As suggested by Rodrigues et al. [40], the dielectric layer heating would be initiated even before the generation of ionic airflow driven by the momentum transfer. Therefore, the response time for the thermal energy generation is expected to be shorter than that of the momentum transfer in plasma discharge. Fig. 5(a) shows the

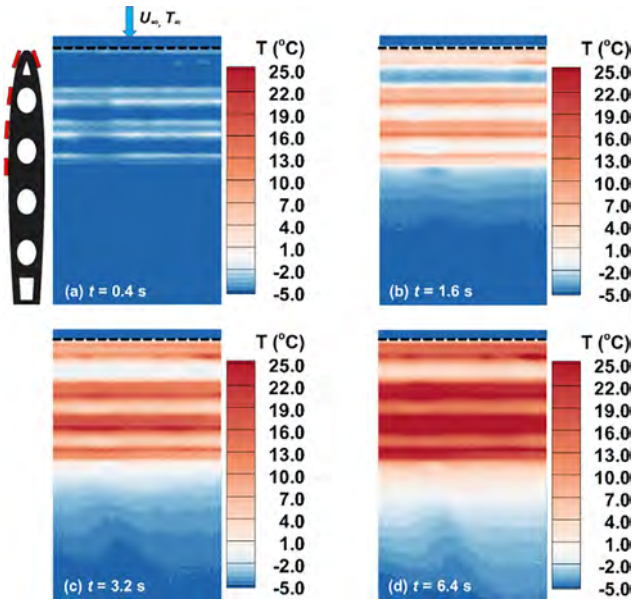

Fig. 5. Time evolution of the measured temperature distribution over the airfoil surface with the DBD plasma actuator operating at $V_{p\text{-}p}$ = 12.5 kV, f = 10 kHz under a dry test condition of U_∞ = 40 m/s, T_∞ = −5°C and LWC = 0 g/m^3.

measured temperature distribution over the airfoil surface right after the DBD plasma actuator was turned on (*i.e.*, t = 0.4 s). It was found that the surface heating was first initiated at the edges of the exposed electrodes with an evident local temperature increase, (*i.e.*, as indicated by the white strips in the temperature map over the airfoil surface), as shown in Fig. 5(a). As the time goes by, more and more thermal energy was generated during the plasma discharge as shown in Fig. 5(b)–(d). It is clearly seen that the maximum temperatures were always located at the edges of the exposed high-voltage electrodes, which agrees with the findings reported in the previous studies [31]. It was also found that, during the plasma discharge, the temperature over the exposed electrodes (*i.e.*, made of copper tape) appeared to be much higher than that over the dielectric layer (*i.e.*, Kapton film). It is suggested that the temperature difference between the electrode surfaces and the dielectric layer surfaces is essentially caused by the significant difference in the thermal conductivity between the copper tape and Kapton film (*i.e.*, 385.0 W/m·K for copper tape *vs.* 1.57 W/m·K for Kapton film). When comparing the surface temperatures at the different discharge locations on the dielectric layer (*i.e.*, spacings between the exposed electrodes) as shown in Fig. 5

(b)–(d), it was found that the surface temperature was the minimum at the leading edge, and increased gradually at further downstream locations, which was due to the chordwise development of convective heat transfer intensity, *i.e.*, with the maximum heat convection being at the leading edge and decreasing gradually in the downstream [42]. It is also found that there is an increasing 3D effect in the surface temperature distribution at the downstream of the plasma actuator, as shown in Fig. 5(c) and (d). Such non-uniformity observed in the downstream temperature distributions is believed to be caused by the slight variations of the thermal behavior along the spanwise direction of the plasma electrodes, which is then amplified along with the development of the thermal boundary layer.

In order to further evaluate the thermal effects of the AC-DBD plasma actuation over the airfoil surface, the span-averaged temperature profiles (with the standard deviation of the spanwise temperature distribution being smaller than 0.5 °C) along the airfoil chord were extracted based on measured temperature distributions over the airfoil surface shown in Fig. 5, and the results were plotted in Fig. 6. The chordwise locations of the exposed electrodes were also illustrated in the plot. It is clearly seen that the temperature profiles at the different time instances have a very similar distribution pattern, *i.e.*, with the temperature peaks being located at the edges of the exposed electrodes. For example, at the time instance of $t = 0.4$ s, while the surface temperatures over the dielectric layer were almost not changed and still below zero, the local temperature peaks at the electrode edges were found to be increased above zero and even becoming higher than 5 °C, as shown in Fig. 6. Along with the rapid temperature rise at the edges of the exposed electrodes, the temperatures over the electrode surfaces were also found to increase significantly, in comparison to that over the dielectric layer. It is well known that the predominant heating mechanism in plasma discharge is due to the heat transfer from the plasma to the gas which then heats up the dielectric surface through forced convection [32]. When the airfoil/wing model with the plasma actuator was exposed in a cold airflow, the hot air generated in plasma discharge region was not only concentrated above the dielectric layer, but also convected over the exposed electrodes. Thus, the temperature increase was also observed over the surfaces of the exposed electrodes. The magnitude of temperature increase over the electrodes/dielectric layer surfaces was essentially determined by the Biot number [42], which is defined as a simple index of the ratio of the heat transfer resistances inside of and at the surface of a body, and usually expressed as:

$$Bi = \frac{L \cdot h}{k} \tag{3}$$

where L is the characteristic length of the body exposed in a fluid, h is the convective heat transfer coefficient of the fluid, and k is the thermal conductivity of the body. A smaller value of the Biot number implies a faster thermal response of the body. Assume the heat convection coefficients at the adjacent electrode and dielectric layer are the same, the thermal response, *i.e.*, surface temperature increase, of the exposed electrode and dielectric layer, can be quantitatively compared by using the following equation:

$$\frac{Bi_{ele}}{Bi_{die}} = \frac{k_{die}}{k_{ele}} \tag{4}$$

where Bi_{ele} is the Biot number for the exposed electrode, Bi_{die} is the Biot number for the dielectric layer, and k_{die} and k_{ele} are the thermal conductivities of the dielectric layer and the exposed electrode, respectively.

Based on the thermal conductivity values given above (*i.e.*, 385.0 W/m·K for copper tape *vs*. 1.57 W/m·K for Kapton film), the ratio of the Biot number between the exposed electrode and dielectric layer was calculated to be $Bi_{ele}/Bi_{die} \approx 0.004$. It indicates that a much faster thermal response (*i.e.*, temperature increase) is expected on the electrode surfaces exposed in the hot air, which is validated by the measured temperature profiles given in Fig. 6.

As the time goes on, the surface temperature of the airfoil/wing model appeared to increase rapidly, with the maximum temperature increased to more than 35 °C after 6.4 s operation of the DBD plasma actuator. It can also be seen clearly in Fig. 6 that, the surface temperature around the third exposed electrode was always higher than those over the other locations, which is suggested to be a result of the development of the thermal boundary layer over the airfoil surface. Since only one-side plasma discharge was actuated at the last electrode (the fourth electrode), the surface temperature at the fourth electrode appeared to be lower than that at the third electrode, with only one temperature peak at the upper edge of the electrode. Further details on the time evolution of the surface temperatures will be discussed in the following sections.

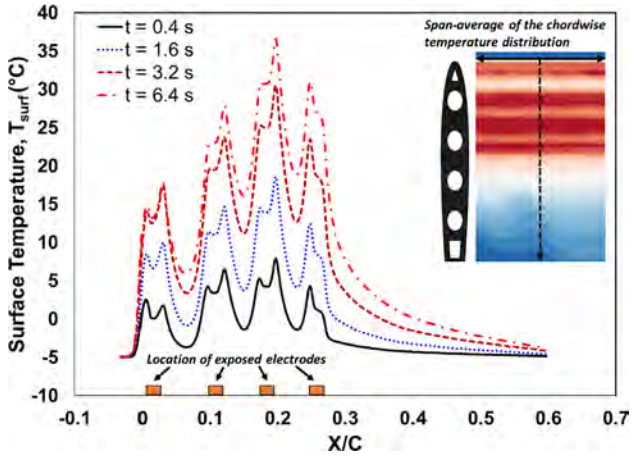

Fig. 6. The spanwise-averaged temperature profiles along the airfoil chord with the DBD plasma actuator operating at $V_{p\text{-}p} = 12.5$ kV, $f = 10$ kHz under a dry test condition of $U_\infty = 40$ m/s, $T_\infty = -5$°C and $LWC = 0$ g/m^3.

3.3. Heat transfer mechanisms during droplet impingement on plasma region and electrical film heater

In looking to compare the AC-DBD plasma actuation and electrical heating method for icing mitigation on the airfoil/wing model, a fundamental understanding of the heat transfer mechanisms during the droplet impingement onto the surface of the plasma actuator (*i.e.*, dielectric surface) and the electrical film heater is highly desirable to elucidate the underlying physics of the complex multiphase interaction before and during the droplet impingement.

Fig. 7 shows the schematics of the heating mechanisms of the impinging droplets on two different surfaces, *i.e.*, electrical film heater *vs.* dielectric layer of the DBD plasma actuator. For the electrical film heater, the thermal energy is generated at the film surface through resistive heating supplied from the electrical power source. Although some of the thermal energy is dissipated to the airflow within the thermal boundary layer through convective heat transfer, which may warm up the impinging droplet before contacting with the hot surface, the dominating heating mechanism for the water droplet is through heat conduction during the dynamic impinging process (*i.e.*, impacting, splashing, and receding), as shown schematically in Fig. 7(a). Due to the large temperature difference between the impinging water droplet and the hot surface, the thermal energy is transferred from the surface into the

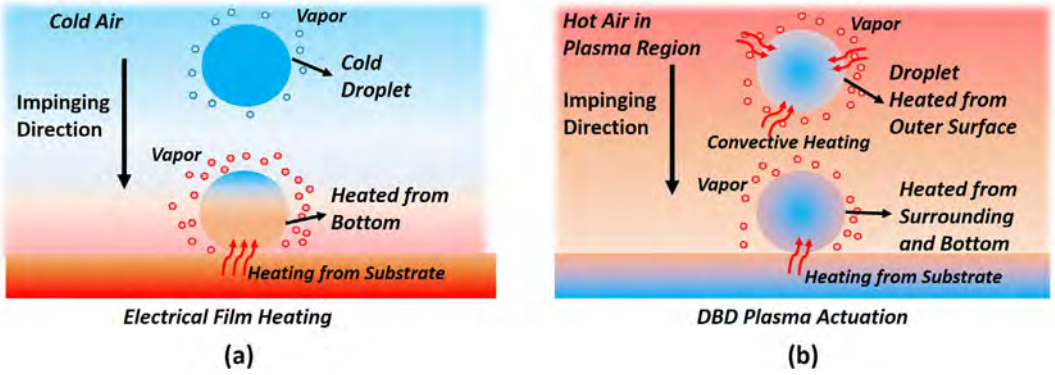

Fig. 7. Heating mechanisms of an impinging droplet on two different surfaces: (a) electrical film heater, (b) dielectric layer of the DBD plasma actuator.

droplet, which can keep the droplet warm (*i.e.*, above the freezing point) or even evaporate upon the impingement of the water droplets onto the surface of the electric film heater.

For the case of the AC-DBD plasma actuation, however, the primary heating mechanism is through heat transfer from the plasma to the ambient gas, which then heats up the dielectric surface through direct injection, convection and radiation [32], which is a reverse thermal path in comparison with that of the conventional electrical heating. Therefore, as the water droplet impinging onto the surface with DBD plasma actuator, the droplet is not only heated up through heat conduction upon in contact with the hot dielectric surface, but also effectively heated up through the forced convective heat transfer when it travels through the hot air in the plasma region, as shown in Fig. 7(b).

As revealed by Li et al. [43], the transient temperature of an in-flight droplet can be calculated using Eq. (5):

$$T = \left[T_i - T_e + T_e \exp\left[(6t_f h)/(\rho c_p D)\right]\right] / \exp\left[(6t_f h)/(\rho c_p D)\right] \quad (5)$$

where T is the transient temperature of the in-flight droplet, h is the convection coefficient of air around the surface of the in-flight droplet, T_i is the initial temperature of the droplet, T_e is the temperature of surrounding air of the droplet, ρ is the density of the droplet, c_p is the specific heat of the droplet; t_f is the time of flight of the droplet in the convective air flow, and D is the diameter of the flying droplet. It is obvious that, for the same time of flight, a higher temperature of the surrounding air would imply a higher transient temperature of the in-flight droplet. Therefore, the temperature of the water droplet before impacting on the surface of the plasma actuator would be much higher than that of impinging onto the electrical film heater.

For the implementations of AC-DBD plasma actuator and electrical film heater for icing mitigation on aircraft, although the heating mechanisms of the two methods are different, they both utilize thermal energy to prevent the impinging supercooled water droplets from being frozen to form ice accretion on the airfoil/wing surfaces. It should be noted that the conventional electrical film heaters usually have almost 100% energy efficiency in the sense that all the input electric energy is converted to thermal energy, while for AC-DBD plasma actuators, the heating efficiency varies from 50% to 90% in different operating conditions [40]. In order to quantitatively evaluate the overall anti-/de-icing performances of the two methods, the total power inputs were always kept identical in the present study to quantitatively compare the DBD plasma-based method with the convention electrical heating method for aircraft icing mitigation.

3.4. Comparison of anti-/de-icing performances of AC-DBD plasma actuator and electrical film heater

In performing the ice accretion experiments, ISU-IRT was operated at a prescribed frozen-cold temperature level (*e.g.*, $T_\infty = -5$ °C for the present study) for at least 60 min in order to ensure ISU-IRT reaching a thermal steady state. Then, the DBD plasma actuator and the electrical film heater embedded over the airfoil/wing surface were switched on for about 60 s to achieve a thermal equilibrium state before turning on the water spray system of ISU-IRT. After the water spray system was switched on at $t = t_0$, while the plasma actuator and the electrical film heater were still in operation, the super-cooled water droplets carried by the incoming airflow would impinge onto the surface of the airfoil/wing model to start the ice accretion process. During the experiments, the high-speed imaging system and the IR thermal imaging system were synchronized to reveal the dynamic ice accretion process and the surface temperature evolution over the ice accreting airfoil/wing model simultaneously.

Fig. 8 shows four typical snapshots of the dynamic ice accretion process over the airfoil surface with the power density of the DBD plasma actuator and the electrical film heater being the same of P_d = 7.8 kW/m^2. The box in red dashed lines in the acquired video images indicates the measurement window of the IR thermal imaging system. Since similar features were also observed for other test cases, only the measurement results obtained under the icing condition of U_∞ = 40 m/s, $T_\infty = -5$ °C and LWC = 1.0 g/m^3 were shown and analyzed here for conciseness. As shown clearly in Fig. 8(a), at the time instance of 10 s after starting the ice accretion experiments, when the supercooled water droplets impinged onto the airfoil surface, since both the DBD plasma actuator and the electrical film heater were switched on with the surface temperatures being well above the freezing point of water, the impinged water droplets were heated up, and no longer in the supercooled state, by absorbing the thermal energy generated due to the plasma actuation and electrical heating. Therefore, the coverage regions of the plasma actuator and the electrical film heater on the airfoil model (*i.e.*, from the leading edge to ~30% chord length) were found to be free of ice, but with evident water runback being observed. Driven by the boundary layer airflow over the airfoil surface, the unfrozen water was found to run back to the further downstream regions in the form of film/rivulet flows. It can be seen clearly that, the runback water started to refreeze in the downstream region after about 60% chord length on the electrical film heater side, while the water runback over the DBD plasma side appeared to be less and only very few ice formation was observed. It is suggested that, at the beginning stage of water impingement, the air over the plasma region was sufficiently

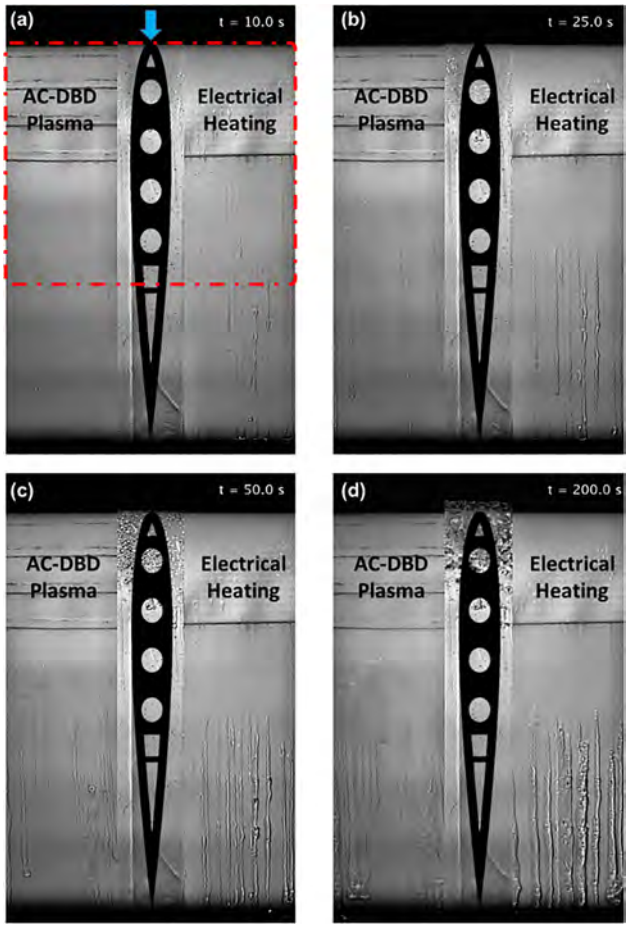

Fig. 8. Typical snapshots of the dynamic ice accretion process with the power density of the plasma actuator and the film heater being P_d = 7.8 kW/m^2 under the icing condition of U_∞ = 40 m/s, T_∞ = −5 °C and LWC = 1.0 g/m^3.

heated which can effectively warm up and evaporate the micro-sized, super-cooled water droplets (*i.e.*, with the diameters less than 100 μm) that traveled through it. For the super-cooled water droplets impinged onto the surface of the electrical film heater, since the thermal energy was mainly transferred from the bottom substrate, and the input power was not sufficiently high to instantly evaporate the water droplets, the impinged water droplets were coalesced quickly to form rivulets/film flows and transported further downstream. The rumback surface water was found to be refrozen to start the ice accretion at the further downstream regions due to the intense convective heat transfer in the frozen cold ambient environment. As the time goes on, more and more super-cooled water droplets impinged onto the surfaces of the DBD plasma actuator and the electrical film heater embedded over the airfoil surface. Since the deposited water film over the dielectric layer/exposed electrodes of the DBD plasma actuator would have a very complex interaction with the plasma actuation [37], which may result in a change of the thermal effects during the plasma discharge, more and more water were found to be collected and transported downstream over the airfoil surface, and started to form ice in the downstream regions, as can be seen in Fig. 8(b). In the meantime, more rivulets-shaped ice formation was observed in the downstream of the electro film heater side. The water/ice rivulets formed in the early stage of the ice accretion (on both plasma and electric film heater sides) became the transport channels for the collected water over the airfoil surface. As the time goes on, more and more impinged water was collected over the airfoil surface, and subsequently frozen at the downstream regions, as shown clearly in Fig. 8(c) and (d).

In order to achieve better anti-/de-icing performances for both the AC-DBD plasma actuator and the electrical film heater under the same icing condition, the power inputs to the DBD plasma actuator and the electrical film heater were increased by a factor of two (*i.e.*, P_d = 15.6 kW/m^2) to generate more thermal energy in the sense of preventing ice formation over the airfoil surface. The typical snapshots of the dynamic water runback/ice accretion process under this operational condition are shown in Fig. 9. It can be clearly seen that, with the higher power input, the airfoil surface was completely free of ice on both sides of the airfoil surface at the early stage of icing experiment (*i.e.*, $t \leq 50$ s) as shown in Fig. 9(a)–(c). Similar to that observed for the case with relatively lower power input described above, the DBD plasma side of the airfoil surface appeared to have less water runback in comparison to that on the electric film heater side. It was also found that the runback speed of the surface water rivulets on the DBD plasma side was slower than that on the electric film heater side, which is suggested to be caused by the different roughness distributions on the two sides of the airfoil surface (*i.e.*, the exposed electrodes of the DBD plasma actuator tend to trap surface water as it runback, while the film heater surface provides a relatively smooth substrate for the surface water runback). Since the slower runback speed of the surface water would allow a longer and more sufficient heat convection to take away the heat from the "warmed" surface water, as more and more water droplets impinged on the

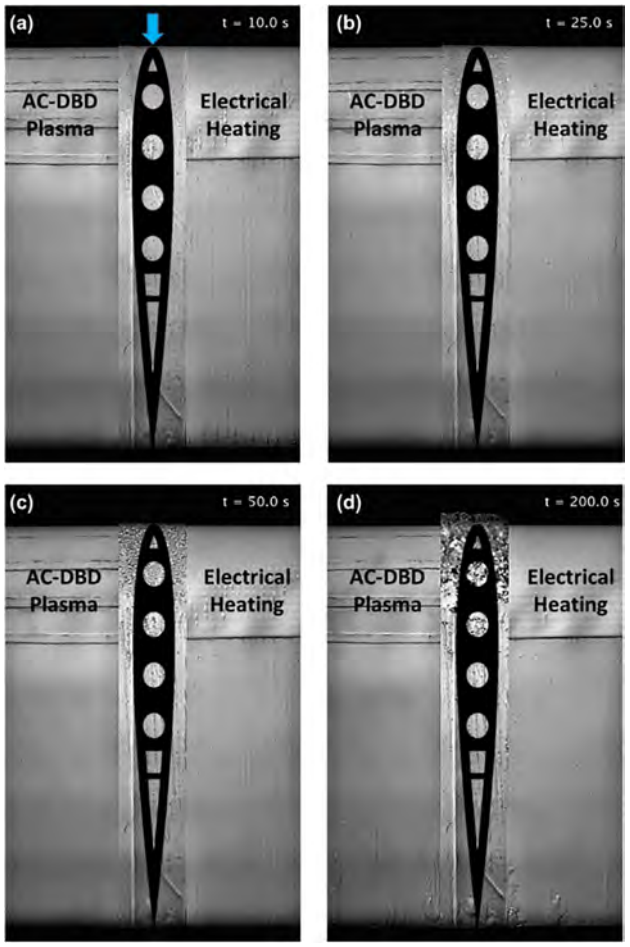

Fig. 9. Typical snapshots of the dynamic ice accretion process with the power density of the plasma actuator and the film heater being P_d = 15.6 kW/m^2 under the icing condition of U_∞ = 40 m/s, T_∞ = −5 °C and LWC = 1.0 g/m^3.

airfoil surface, ice was found to form at a nearer downstream location on the DBD plasma side after about t = 200 s after starting the icing experiments, as shown in Fig. 9(d).

Fig. 10 shows the time evolution of the measured temperature distributions over the airfoil surface with the power density being kept constant at P_d = 15.6 kW/m^2 on both sides of the airfoil before and during the ice accretion process under the icing condition of U_∞ = 40 m/s, T_∞ = −5 °C and LWC = 1.0 g/m^3. The corresponding surface temperature variations at different chordwise locations (*i.e.*, location A at 2% chord, B at 10% chord, C at 18% chord, D at 45% chord, as indicated in Fig. 10(a)) on the two sides (*i.e.*, plasma actuator side *vs.* electric film heater side) of the airfoil surface are also shown in Fig. 11. As can be seen clearly in Fig. 10(a), after the DBD plasma actuator was enabled for 10 s (*i.e.*, at t = 10 s), the temperatures over the surfaces of the exposed electrodes were found to increase to about 10 °C, while the temperatures over the dielectric surface (*i.e.*, the spacings between the electrodes) were still kept below zero (*i.e.*, the freezing point of water), which has been discussed in the previous section. The electrical film heater was enabled simultaneously with the DBD plasma actuator during the experiment. It was found that there was a strip-patterned temperature distribution over the electric film heater at t = 10 s, as shown in Fig. 10(a). Such strip-like temperature distribution was essentially due to the configuration of the etched foil resistance element encapsulated between the Polyimide films in the electric heater. As the time goes on, more and more thermal energy was generated on both the plasma actuator side and the electric film heater side of the airfoil surface. After running the plasma actuator and the electric film heater for about 60 s, a thermal equilibrium state was achieved on both sides of the airfoil/wing model as indicated by the flattening surface temperature profiles at t = 60 s, as shown in Fig. 11(a) and (b). At this thermal equilibrium state, it was found that the temperature distribution on the electrical film heater was much higher than that over the DBD plasma actuators, as clearly shown in Fig. 10(b). The temperatures at the location "C" (*i.e.*, 18% chord) were found to be the maximum on both sides, with the measured values being 20 °C and 90 °C on the plasma actuator side and the electric film heater side, respectively. As described above, while the thermal energy generated by the electrical film heater is mainly at the heater surface through resistive heating, the primary heating mechanism in DBD plasma actuation is through heat transfer from the plasma to the ambient gas, which then heats up the dielectric/electrodes surfaces through direct injection, convection and radiation [32]. Therefore, with the same power input, the measured surface temperature on the electric film heater surface appeared to be much higher than that over the DBD plasma actuator. It was also found that, after the thermal equilibrium state was achieved, the temperature appeared to be higher at locations further away from the airfoil leading edge (until location C at 18% chord length) as clearly shown in Figs. 10 and 11. Such a temperature gradient was believed to be due to the development of the thermal boundary layer over the airfoil surface, with

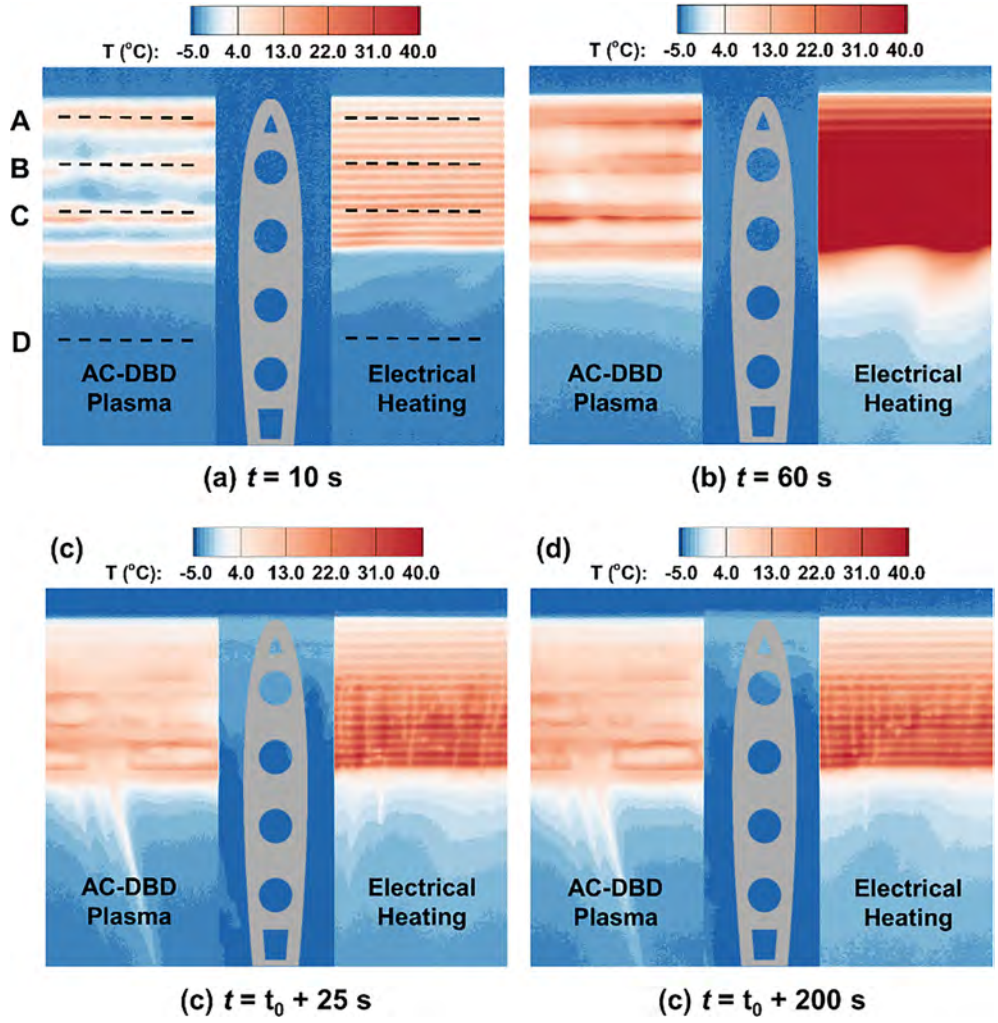

Fig. 10. Time evolution of the temperature distributions over the DBD plasma and film heater sides of the airfoil surface with the input power density being P_d = 15.6 kW/m^2 before (*i.e.*, (a) and (b)) and during (*i.e.*, (c) and (d)) the ice accretion process at U_∞ = 40 m/s, T_∞ = −5 °C and LWC = 1.0 g/m^3.

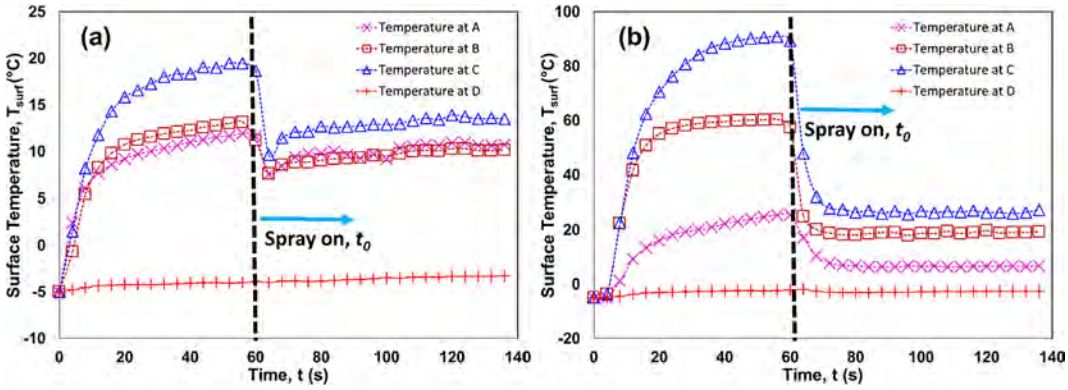

Fig. 11. Surface temperature variations at different chordwise locations on (a) the plasma side and (b) the electric film heater side of the airfoil surface before and during the ice accretion process at U_∞ = 40 m/s, T_∞ = −5 °C and LWC = 1.0 g/m^3. The power density applied to both the plasma actuator and film heater being kept at the same level of P_d = 15.6 kW/m^2.

the maximum heat convection at the airfoil leading edge and decreasing gradually in the downstream region.

As indicated by the dashed line in Fig. 11, the water spray system of ISU was switched on at t = 60 s to start the ice accretion process, *i.e.*, 60 seconds after the plasma actuator and the electrical film heater were enabled. This time instant was also defined as t_0, as given in Fig. 10(c) and (d). It was found that, after the super-cooled water droplets impinged onto the airfoil surface, for the time instance at $t = t_0 + 25$ s, while the surface temperature on the electric film heater was found to decrease significantly, the temperature on the surface of the plasma actuator only dropped slightly as shown in Fig. 10(c). As the time goes on, more and more impinged water would be collected on the airfoil surface. Since the power input to the plasma actuator and the electric film heater were sufficiently high to prevent ice accretion over the airfoil surfaces, the mass transport and energy transfer on the two sides of the airfoil surface were found to reach an equilibrium state, as indicated by the almost unchanged temperature distributions after $t = t_0 + 200$ s, as shown in Fig. 10(d). More quantitatively, after the water droplets impinged on the airfoil surface, while the temperature drop on the surface of the plasma actuator was about 33% (*i.e.*, the temperature dropped from 12 °C to 8 °C at the location A and B, and dropped from 18 °C to 12 °C at the location C) as shown in Fig. 11(a), the temperature decrease on the surface of the electrical film heater was found to be around 70% (*i.e.*, the temperature decreased from 25 °C to 6 °C at the location A, from 60 °C to 20 °C at the location B, and from 90 °C to 25 °C at the location C) as shown in Fig. 11(b). Such temperature variations before and after the impingement of the super-cooled water droplets can be explained by the different heating mechanisms discussed in the previous section. For the electrical film heater case, since the thermal energy was mainly generated at the heater surface, and then transferred into the impinged supercooled water droplets upon impact, the measured surface temperature, therefore, appeared to drop significantly when the temperature different was large between the heater surface and the impinged water droplets. For the droplet impingement on the surface of the DBD plasma actuator, however, the droplets had already been effectively warmed up through the forced heat convection as travelling through the hot air above the plasma actuator before impacting onto the warm dielectric/electrodes surface.

3.5. Further optimization of AC-DBD plasma actuation for improved icing mitigation performance

Based on the measurement results described above, it can be concluded that, the DBD plasma-based method is very promising and have a great potential for aircraft icing mitigation. With the same power input, the DBD plasma-based method was found to have at least equivalent effectiveness, if not better, in preventing ice accretion over the airfoil surface, in comparison with the conventional electrical heating method. It should be noted that, the anti-/de-icing performance of the DBD plasma-based method can be further improved through optimization of the design paradigms in the terms of the geometry of the plasma actuator, the area of the plasma actuation over the airfoil surface, the effects of the applied voltage and frequency, etc. As an example of the attempts to optimize the DBD plasma actuation for improved anti-/de-icing performance, a duty-cycled modulation concept is utilized by leveraging the unique feature of fast response time for the DBD plasma actuation (*i.e.*, on the order of 10–100 ms) in terms of momentum transfer [41] and thermal effects [40] induced by plasma discharge. Thus, with the same total power input applied to the DBD plasma actuator, the maximum instantaneous power input applied to the plasma actuator can be significantly increased by adopting the duty-cycled modulation. In the present study, an explorative study was also performed to evaluate the anti-/de-icing performance of the plasma actuation with duty-cycled modulation, in comparison to that of the conventional electrical heating method with the same total power input, under the same icing condition (*i.e.*, U_∞ = 40 m/s, T_∞ = −5 °C and LWC = 1.0 g/m^3).

Fig. 12 shows four typical snapshots of the dynamic ice accretion process over the airfoil surface with the maximum instantaneous input power density of the duty-cycled plasma actuation (*i.e.*, with a duty cycle of τ = 50% at the frequency of $f_{duty\text{-}cycle}$ = 250 Hz) being P_d = 15.6 kW/m^2, while the power density of the conventional electric film heater was kept at P_d = 7.8 kW/m^2. In this comparison, although the maximum instantaneous power inputs were different for the DBD plasma actuator and the electrical film heater, the total power consumptions over a given period of time would remain the same. It can be seen clearly in Fig. 12(a) that, when the super-cooled water droplets impinged onto the airfoil surface, since both the DBD plasma side and the electric film heater side were heated up, the impinged super-cooled water droplets would be heated up instantly upon impact, with the temperature of the impinged water increased above zero (*i.e.*, above the frozen point of water) and no longer in super-cooled state. Consequently, the impinged water droplets quickly coalesced and run back in the form of film/rivulet flows as driven by the boundary layer airflow over the airfoil surface, as shown in Fig. 12(a). It was found that the runback surface water on the plasma side was much lesser than that on the electric film heater side, which is suggested to be caused by the more significant evaporation of the impinged water droplets over the airfoil surface with plasma actuation. As the time goes on, more and more

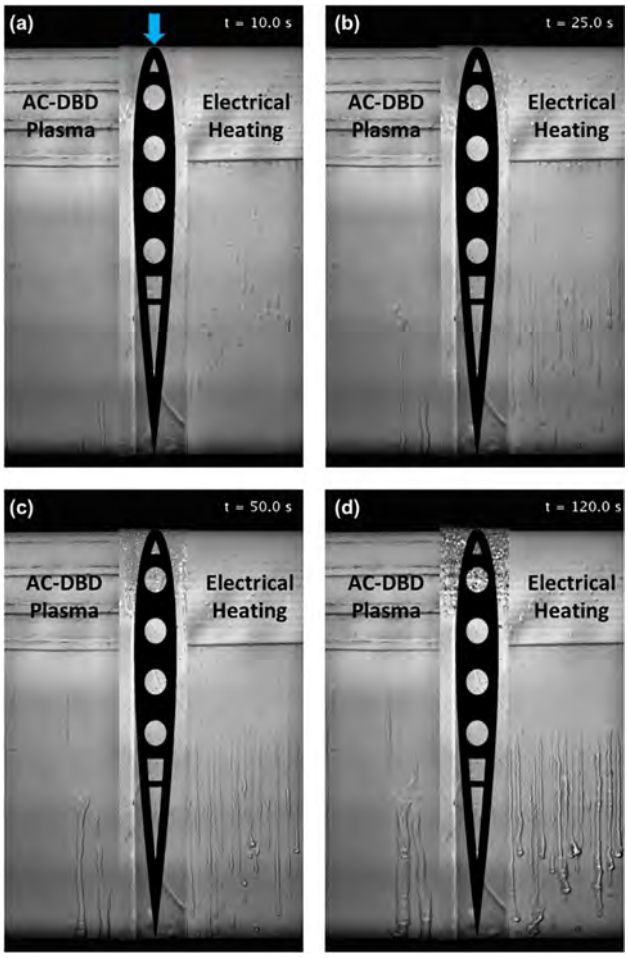

Fig. 12. Typical snapshots of the dynamic ice accretion process over the airfoil surface under the icing condition of U_∞ = 40 m/s, T_∞ = −5 °C and LWC = 1.0 g/m^3 with the duty-cycled plasma actuation (*i.e.*, with a duty cycle of τ = 50% at the frequency of $f_{duty\text{-}cycle}$ = 250 Hz) on the left side and the electric film heating on the right side.

water droplets impinged onto the airfoil surface with more water runback appeared in the downstream region (*i.e.*, after 50% chord length) as shown in Fig. 12(b). Since the temperature of the surface water was not sufficiently high, the heat stored in the runback water was rapidly removed by the intense heat convection during the runback process, therefore, the rivulets-shaped ice was found to form at the further downstream region as clearly seen in Fig. 12(c)–(d). It should be noted that, although both sides of the airfoil surface had ice formation in the downstream region, much less ice accretion was found on the plasma side of the airfoil surface in comparison to that on the electric film heater side. It is suggested that, with the same total power input, the DBD plasma actuation with the duty-cycle modulation would have a better anti-/de-icing performance in comparison to that of the conventional electrical film heater.

4. Conclusion

In the present study, an experimental investigation was performed to compare the effectiveness of a novel DBD plasma-based method with a conventional electrical heating method in preventing ice formation and accretion over an airfoil/wing model in order to demonstrate the great potential of utilizing DBD plasma actuators for aircraft in-flight icing mitigation. The experimental study was performed in the Icing Research Tunnel available at Aerospace Engineering Department of Iowa State University (*i.e.*, ISU-IRT). A NACA0012 airfoil/wing model embedded with a DBD plasma actuator and a conventional electrical film heater over the airfoil surface was tested in the ISU-IRT under a typical glaze icing condition. During the experiments, while a high-speed imaging system was used to record the dynamic ice accretion and transient surface water runback processes over the airfoil surface, an infrared (IR) thermal imaging system was also utilized to map the corresponding temperature distributions over the ice accreting airfoil surface simultaneously. Based on the side-by-side comparison of the measurement results (*i.e.*, snapshots of the visualization images and quantitative surface temperature distributions) on the plasma side of the airfoil surface against those of the electric film heater side under the same icing condition, the effectiveness of using the thermal effects induced by DBD plasma actuation and the conventional electrical heating in preventing ice formation and accretion over the airfoil surface was evaluated and analyzed in details.

It was found that, with the same input power density, the surface temperature on the electric film heater was much higher than that over the surface of the DBD plasma actuator before the water droplets impingement, which was essentially due to the different heating mechanisms of the two methods. For the conventional electrical film heater, the thermal energy was mainly generated at the heater surface. For the case of the DBD plasma actuation, the heating path is through heat transfer from the plasma to the ambient gas at first, and then heats up the surfaces of the dielectric layer and electrodes of the plasma actuator through direct injection, convection and radiation. Upon the impingement of the super-cooled water droplets onto the airfoil surface, while the surface temperature over the electrical film heater was found to drop significantly due to the instant heat transfer from the electric film heater surface to the impinged water mass, the decrease in the measured surface temperature over the plasma side appeared to be much less since the impinged water droplets were not only heated up through heat conduction upon in contact with the hot dielectric/electrodes surfaces, but also effectively warmed up through forced heat convection as they travelling through the hot air above the DBD plasma actuator. As a result, the DBD plasma-based method showed a more promising performance in preventing the ice formation and accretion over the airfoil surface, in comparison with that of the conventional electrical heating method.

An explorative study was also conducted to further improve the anti-/de-icing performance of the DBD plasma-based method by adopting a duty-cycle modulation concept. The implementation of duty-cycled modulation to the DBD plasma actuation can significantly reduce the total power consumption of the plasma actuator over time (*e.g.*, 50% energy can be saved when using a duty cycle modulation of τ = 50%), while maintaining the same maximum instantaneous power input applied to the DBD plasma actuator for anti-/de-icing operation. Based on the side-by-side comparison of the measurement results obtained under the same icing condition and the same total power input, it was demonstrated clearly that, the duty-cycled plasma actuation have a better anti-/de-icing performance in comparison to the conventional electrical heating method.

Conflict of interest

The authors declared that there is no conflict of interest.

Acknowledgments

The research work is partially supported by Iowa Space Grant Consortium (ISGC) Base Program for Aircraft Icing Studies and

National Science Foundation (NSF) under award numbers of CBET-1064196 and CBET-1435590. The technical assistance of Dr. Xuanshi Meng of Northwestern Polytechnic University is greatly appreciated.

References

[1] K. Petty, C. Floyd, A statistical review of aviation airframe icing accidents in the US, in: Proc. 11th Conf. Aviat. Range, Aerosp. Hyannis, 2004.

[2] R.W. Gent, N.P. Dart, J.T. Cansdale, Aircraft icing, Philos. Trans. R. Soc. London. Ser. A Math. Phys. Eng. Sci. 358 (1776) (2000) 2873–2911.

[3] M. Bragg, G. Gregorek, J. Lee, Airfoil aerodynamics in icing conditions, J. Aircr. 23 (1) (1986) 76–81.

[4] T. Cebeci, F. Kafyeke, Aircraft icing, Annu. Rev. Fluid Mech. 35 (2003) 11–21.

[5] Y. Liu, W.-L. Chen, L.J. Bond, H. Hu, An experimental study on the characteristics of wind-driven surface water film flows by using a multi-transducer ultrasonic pulse-echo technique, Phys. Fluids 29 (1) (2017) 12102, https://doi.org/10.1063/1.4973398.

[6] Y. Liu, H. Hu, An experimental investigation on the unsteady heat transfer process over an ice accreting airfoil surface, Int. J. Heat Mass Transf. 122 (2018) 707–718, https://doi.org/10.1016/j.ijheatmasstransfer.2018.02.023.

[7] R.M. Waldman, H. Hu, High-speed imaging to quantify transient ice accretion process over an airfoil, J. Aircr. 53 (2) (2015) 369–377, https://doi.org/10.2514/1.C033367.

[8] G. Fortin, J.-L. Laforte, A. Ilinca, Heat and mass transfer during ice accretion on aircraft wings with an improved roughness model, Int. J. Thermal Sci. 45 (6) (2006) 595–606, https://doi.org/10.1016/j.ijthermalsci.2005.07.006.

[9] Y. Liu, L. Li, Z. Ning, W. Tian, H. Hu, Experimental investigation on the dynamic icing process over a rotating propeller model, J. Propuls Power. (2018) 1–14, https://doi.org/10.2514/1.B36748.

[10] S.K. Thomas, R.P. Cassoni, C.D. MacArthur, Aircraft anti-icing and de-icing techniques and modeling, J. Aircr. 33 (5) (1996) 841–854, https://doi.org/10.2514/3.47027.

[11] Y. Liu, L. Li, H. Li, H. Hu, An experimental study of surface wettability effects on dynamic ice accretion process over an UAS propeller model, Aerosp. Sci. Technol. 73 (2018) 164–172, https://doi.org/10.1016/j.ast.2017.12.003.

[12] Y. Liu, L.J. Bond, H. Hu, Ultrasonic-attenuation-based technique for ice characterization pertinent to aircraft icing phenomena, AIAA J. 55 (5) (2017) 1602–1609, https://doi.org/10.2514/1.J055500.

[13] D.M. Ramakrishna, T. Viraraghavan, Environmental impact of chemical deicers – a review, Water. Air. Soil Pollut. 166 (1–4) (2005) 49–63, https://doi.org/10.1007/s11270-005-8265-9.

[14] L. Gray, Review of aircraft deicing and anti-icing fluid storm water runoff control technologies, in: Air and Water Pollution Prevention, 2013, p. MANE 6960H01.

[15] R. Kent, D. Andersen, Canadian water quality guidelines for glycols–An ecotoxicological review of glycols and associated aircraft anti-icing and deicing fluids, Environ. Toxicol. 14 (5) (1999) 481–522.

[16] S.K. Thomas, R.P. Cassoni, C.D. MacArthur, Aircraft anti-icing and de-icing techniques and modeling, J. Aircr. 33 (5) (2012) 841–854.

[17] T.C. Corke, C.L. Enloe, S.P. Wilkinson, Dielectric barrier discharge plasma actuators for flow control, Annu. Rev. Fluid Mech. 42 (2010) 505–529, https://doi.org/10.1146/annurev-fluid-121108-145550.

[18] F.O. Thomas, T.C. Corke, M. Iqbal, A. Kozlov, D. Schatzman, Optimization of dielectric barrier discharge plasma actuators for active aerodynamic flow control, AIAA J. 47 (9) (2009) 2169–2178, https://doi.org/10.2514/1.41588.

[19] D.V. Roupassov, A.A. Nikipelov, M.M. Nudnova, A.Y. Starikovskii, Flow separation control by plasma actuator with nanosecond pulsed-periodic discharge, AIAA J. 47 (1) (2009) 168–185, https://doi.org/10.2514/1.38113.

[20] G. Correale, T. Michelis, D. Ragni, M. Kotsonis, F. Scarano, Nanosecond-pulsed plasma actuation in quiescent air and laminar boundary layer, J. Phys. D. Appl. Phys. 47 (10) (2014) 105201, https://doi.org/10.1088/0022-3727/47/10/105201.

[21] M. Samimy, J.-H. Kim, J. Kastner, I. Adamovich, Y. Utkin, Active control of high-speed and high-Reynolds-number jets using plasma actuators, J. Fluid Mech. 578 (2007) 305, https://doi.org/10.1017/S0022112007004867.

[22] N.L. Aleksandrov, S.V. Kindysheva, M.M. Nudnova, A.Y. Starikovskiy, Mechanism of ultra-fast heating in a non-equilibrium weakly ionized air discharge plasma in high electric fields, J. Phys. D. Appl. Phys. 43 (25) (2010) 255201, https://doi.org/10.1088/0022-3727/43/25/255201.

[23] J. Little, K. Takashima, M. Nishihara, I. Adamovich, M. Samimy, Separation control with nanosecond-pulse-driven dielectric barrier discharge plasma actuators, AIAA J. 50 (2) (2012) 350–365, https://doi.org/10.2514/1.J051114.

[24] N. Benard, E. Moreau, On the vortex dynamic of airflow reattachment forced by a single non-thermal plasma discharge actuator, flow, Turbul. Combust. 87 (1) (2011) 1–31, https://doi.org/10.1007/s10494-011-9325-4.

[25] J. Little, M. Nishihara, I. Adamovich, M. Samimy, High-lift airfoil trailing edge separation control using a single dielectric barrier discharge plasma actuator, Exp. Fluids 48 (3) (2010) 521–537, https://doi.org/10.1007/s00348-009-0755-x.

[26] R. Joussot, D. Hong, R. Weber-Rozenbaum, A. Leroy-Chesneau, Modification of the laminar-to-turbulent transition on a flat plate using DBD plasma actuator, in: 5th Flow Control Conf., American Institute of Aeronautics and Astronautics, 2010. http://doi.org/10.2514/6.2010-4708.

[27] A. Duchmann, S. Grundmann, C. Tropea, Delay of natural transition with dielectric barrier discharges, Exp. Fluids 54 (2013) 1461, https://doi.org/10.1007/s00348-013-1461-2.

[28] W. Zhou, Y. Liu, H. Hu, H. Hu, X. Meng, Utilization of thermal effect induced by plasma generation for aircraft icing mitigation, AIAA J. 56 (2018) 1097–1104, https://doi.org/10.2514/1.J056358.

[29] S.A. Stanfield, J. Menart, C. DeJoseph, R.L. Kimmel, J.R. Hayes, Rotational and vibrational temperature distributions for a dielectric barrier discharge in air, AIAA J. 47 (5) (2009) 1107–1115, https://doi.org/10.2514/1.37648.

[30] B. Dong, J.M. Bauchire, J.M. Pouvesle, P. Magnier, D. Hong, Experimental study of a DBD surface discharge for the active control of subsonic airflow, J. Phys. D. Appl. Phys. 41 (15) (2008) 155201, https://doi.org/10.1088/0022-3727/41/15/155201.

[31] R. Joussot, V. Boucinha, R. Weber-Rozenbaum, H. Rabat, A. Leroy-Chesneau, D. Hong, Thermal characterization of a DBD plasma actuator: dielectric temperature measurements using infrared thermography, in: 40th Fluid Dyn. Conf. Exhib., American Institute of Aeronautics and Astronautics, Chicago, Illinois, 2010. http://doi.org/10.2514/6.2010-5102.

[32] R. Tirumala, N. Benard, E. Moreau, M. Fenot, G. Lalizel, E. Dorignac, Temperature characterization of dielectric barrier discharge actuators: influence of electrical and geometric parameters, J. Phys. D. Appl. Phys. 47 (25) (2014) 255203, https://doi.org/10.1088/0022-3727/47/25/255203.

[33] J. Van den Broecke, Efficiency and de-icing capability of nanosecond pulsed dielectric barrier discharge plasma actuators, Master thesis, Delft University of Technology, 2016.

[34] S.M. Soloff, R.J. Adrian, Z.-C. Liu, Distortion compensation for generalized stereoscopic particle image velocimetry, Meas. Sci. Technol. 8 (12) (1997) 1441–1454, https://doi.org/10.1088/0957-0233/8/12/008.

[35] R. Joussot, V. Lago, J.-D. Parisse, Quantification of the effect of surface heating on shock wave modification by a plasma actuator in a low-density supersonic flow over a flat plate, Exp. Fluids 56 (2015) 102, https://doi.org/10.1007/s00348-015-1970-2.

[36] L. Li, H. Hu, An Experimental study of dynamic ice accretion process on aero-engine spinners, in: 55th AIAA Aerosp. Sci. Meet., American Institute of Aeronautics and Astronautics, 2017. http://doi.org/10.2514/6.2017-0551.

[37] S.B. Leonov, V. Petrishchev, I.V. Adamovich, Dynamics of energy coupling and thermalization in barrier discharges over dielectric and weakly conducting surfaces on μs to ms time scales, J. Phys. D. Appl. Phys. 47 (46) (2014) 465201, https://doi.org/10.1088/0022-3727/47/46/465201.

[38] Y. Zhu, Y. Wu, W. Cui, Y. Li, M. Jia, Numerical investigation of energy transfer for fast gas heating in an atmospheric nanosecond-pulsed DBD under different negative slopes, J. Phys. D. Appl. Phys. 46 (49) (2013) 495205, https://doi.org/10.1088/0022-3727/46/49/495205.

[39] H. Conrads, M. Schmidt, Plasma generation and plasma sources, Plasma Sources Sci. Technol. 9 (4) (2000) 441–454, https://doi.org/10.1088/0963-0252/9/4/301.

[40] F. Rodrigues, J. Pascoa, M. Trancossi, Heat generation mechanisms of DBD plasma actuators, Exp. Thermal Fluid Sci. 90 (2018) 55–65, https://doi.org/10.1016/j.expthermflusci.2017.09.005.

[41] N. Benard, E. Moreau, Electrical and mechanical characteristics of surface AC dielectric barrier discharge plasma actuators applied to airflow control, Exp. Fluids 55 (2014) 1846, https://doi.org/10.1007/s00348-014-1846-x.

[42] F.P. Incropera, Fundamentals of Heat and Mass Transfer, John Wiley & Sons, 2011.

[43] H. Li, F. Chen, H. Hu, Simultaneous measurements of droplet size, flying velocity and transient temperature of in-flight droplets by using a molecular tagging technique, Exp. Fluids 56 (2015) 194, https://doi.org/10.1007/s00348-015-2063-y.